ROYAL SOCIETY
OF CHEMISTRY

EDGE ARTICLE

Check for updates

Ruthenium clusters decorated on lattice expanded hematite Fe₂O₃ for efficient electrocatalytic alkaline water splitting†

Haibin Ma,‡[a] Yongqiang Yang,‡[b] Xiaohua Yu, [ID] ‡[c] Yang Zhao,[d] Jiwei Ma [ID] *[a] and Hongfei Cheng [ID] *[a]

Electrocatalytic water splitting in alkaline media plays an important role in hydrogen production technology. Normally, the catalytic activity of commonly used transition metal oxides usually suffers from unsatisfactory electron conductivity and unfavorable binding strength for transition intermediates. To boost the intrinsic catalytic activity, we propose a rational strategy to construct lattice distorted transition metal oxides decorated with noble-metal nanoclusters. This strategy is verified by loading ruthenium clusters onto lithium ion intercalated hematite Fe₂O₃, which leads to significant distortion of the FeO₆ unit cells. A remarkable overpotential of 21 mV with a Tafel slope of 39.8 mV dec⁻¹ is achieved at 10 mA cm⁻² for the hydrogen evolution reaction in 1.0 M KOH aqueous electrolyte. The assembled alkaline electrolyzer can catalyse overall water splitting for as long as 165 h at a current density of 250 mA cm⁻² with negligible performance degradation, indicating great potential in the field of sustainable hydrogen production.

Introduction

Electrocatalytic water splitting in alkaline media provides an important and practical technique for sustainable hydrogen production.[1–3] The performance of this technology highly depends on the intrinsic activity of catalysts.[3–8] Normally, the overall water splitting process includes the hydrogen evolution reaction (HER) occurring on the cathode and the oxygen evolution reaction (OER) occurring on the anode.[9,10] Construction of bifunctional catalysts towards the above two reactions can simplify the catalyst preparation process and thus is an economic strategy for electrochemical hydrogen production.[11] The kinetics of the HER process is largely hindered by the water molecule dissociation step, also called the Volmer step;[12,13] whereas the kinetics of the OER process is seriously limited by the unfavorable adsorption of oxygen intermediates on

catalysts.[14,15] Currently, the commonly used catalysts in this field are mainly transition metal oxides due to their capacity to cleave water molecules and suitable adsorption for hydroxyl ions.[16] However, the large-scale application of transition metal oxides is hindered by their unsatisfactory electron conductivity, especially at large current densities. Furthermore, the intrinsic activity of these catalysts is limited by the unfavorable binding strength for transition intermediates during electrochemical reactions, which makes the practical industrial application of these catalysts more challenging.[17,18]

Constructing transition metal oxide-based heterostructures modulated by interface engineering has been demonstrated to promote charge transfer recently.[19,20] It is generally recognized that transition metal oxides serving as a support in heterostructures can also act as co-catalysts toward water splitting. However, some intrinsic properties of transition metal oxides hinder their function in electrochemical water splitting. These properties include low electron conductivity, unsatisfactory metal–support interaction, and strong binding strength with adsorbed hydrogen species. Fortunately, introducing lattice distortion in transition metal oxides can be an efficient strategy to form crystal defects;[21–23] thus, more active sites were generated in the interfacial region, and the interaction between the metal and metal oxide support can be strengthened. Lithiation of metal oxides is a commonly used strategy to realize lattice distortion.[24–26] Previous work has reported a commonly used lithiation method based on the lithium battery discharging technique.[27] However, this method is difficult and time-consuming to operate, and the yield of the targeted product is

[a] *Shanghai Key Laboratory for R&D and Application of Metallic Functional Materials, Institute of New Energy for Vehicles, School of Materials Science and Engineering, Tongji University, Shanghai 201804, China. E-mail: cheng_hongfei@tongji.edu.cn; jiwei.ma@tongji.edu.cn*

[b] *Shenyang National Laboratory for Materials Science, Institute of Metal Research, Chinese Academy of Sciences, Shenyang 110016, China*

[c] *Faculty of Materials Science and Engineering, Kunming University of Science and Technology, Kunming 650093, China*

[d] *Dalian National Laboratory for Clean Energy (DNL), Dalian Institute of Chemical Physics, Chinese Academy of Science, Dalian 116023, China*

† Electronic supplementary information (ESI) available: Materials and methods and additional tables and figures. See DOI: https://doi.org/10.1039/d4sc06732k

‡ These authors contributed equally to this work.

usually very low.[28] Herein, we developed a novel electrochemical method to realize lithiation, which is easy and time-saving to operate. As for the unfavorable binding strength with adsorbed hydrogen species, we introduced ruthenium (Ru) clusters to be responsible for hydrogen molecule formation, *i.e.* the Heyrovsky or Tafel step for alkaline HER.[19] The weak interaction between Ru clusters and adsorbed hydrogen species can effectively promote HER catalysis. In addition, the Ru clusters decorated on lattice distorted transition metal oxides can efficiently modulate the electronic structure of active sites; thus, the interaction with oxygen intermediates in alkaline OER can be modulated.

On the basis of the above description, this work reports a novel bifunctional catalyst for electrocatalytic water splitting in alkaline media, which consists of lithium-intercalated hematite Fe_2O_3 decorated with Ru nanoclusters. In 1.0 M KOH electrolyte, this catalyst only requires an overpotential of 21 mV associated with a durability of 700 h at 10 mA cm^{-2} toward the HER and an overpotential of 328 mV associated with a durability of 190 h at 250 mA cm^{-2} toward the OER. When this
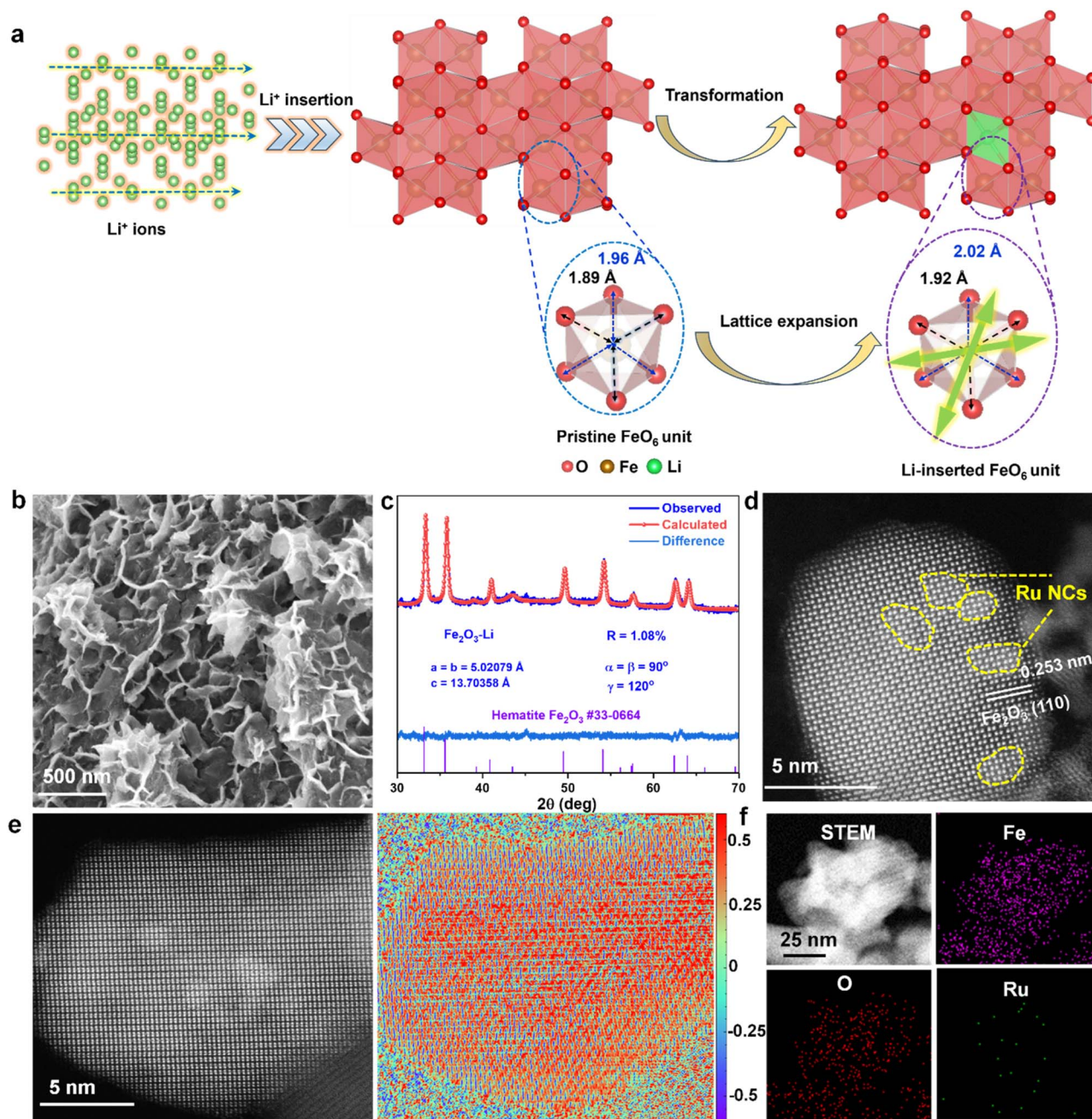

Fig. 1 Atomic structure. (a) Schematic illustration for the lattice expansion effect of hematite Fe_2O_3 after Li ion insertion. (b) Typical SEM image of Fe_2O_3–Li. (c) Refined XRD pattern of Fe_2O_3–Li. (d) HAADF-STEM images of Ru/Fe_2O_3–Li. (e) HAADF-STEM image of Ru/Fe_2O_3–Li and the corresponding lattice distortion analysis by the GPA method. (f) STEM image of Ru/Fe_2O_3–Li and the corresponding EDS elemental mapping images of Fe, O, and Ru species.

catalyst is assembled into traditional two-electrode electrolyzers, the system only requires a voltage of 1.68 V to drive a current density of 100 mA cm^{-2} and exhibits remarkable stability in alkaline media. The theoretical simulation results suggest that the band gap of hematite Fe_2O_3 narrowed after lithium ion intercalation, and the electronic interaction between Ru nanoclusters and lithium-ion intercalated hematite Fe_2O_3 efficiently reduced the energy barrier of water dissociation in alkaline HER, thus synergistically promoting electrocatalytic hydrogen production.

Results and discussion

Materials characterization

To prepare lithium ion inserted hematite Fe_2O_3, Fe_2O_3 was used as the working electrode (WE) and 7.5 mM LiOH aqueous solution was used as the electrolyte. The lithiation was achieved by imposing negative potential on the WE at a constant current density of -1.0 mA cm^{-2} for 5 min. As illustrated in Fig. 1a, Li$^+$ ions transport to the nearby hematite Fe_2O_3 driven by the Coulomb force under an electric field. Since Li ions have a larger radius than Fe^{3+} ions, the volume of the FeO_6 unit cell will be slightly enlarged to accommodate Li ions.

To investigate the effect of lithiation on the physical properties of hematite Fe_2O_3, we performed molecular kinetics simulation based on density functional theory (DFT). The theoretical calculation results in Fig. S1† show that the band

gap of semiconductor hematite Fe_2O_3 narrowed from 0.51 eV to 0.48 eV, indicating improved electron conductivity[29] after Li ion insertion, which is beneficial for electrocatalysis.

Before lithium intercalation, the hematite Fe_2O_3 has nanosheet morphology with irregular orientation (Fig. S2a).† The refined X-ray diffraction (XRD) pattern in Fig. S2b† displays the basic crystal parameters of hematite Fe_2O_3: $a = b = 5.00927$, $c = 13.66199$; $\alpha = \beta = 90°$, $\gamma = 120°$. The high-resolution transmission electron microscopy (HRTEM) image in Fig. S2c† shows that the Fe_2O_3 nanosheet has good crystallinity with a lattice spacing of 0.251 nm, corresponding to the (110) plane. After approaching 0.75 wt% (obtained from inductively coupled plasma-optical emission spectrometer (ICP-OES) analysis) Li ion intercalation, the nanosheet morphology retained (Fig. 1b), while the volume of the hematite Fe_2O_3 unit cell increased by about 0.7% (Fig. 1c). After Li insertion, the XRD peaks shifted to smaller angles, further consolidating the above analysis (Fig. S3†).

The Ru cluster decoration on Li ion intercalated hematite Fe_2O_3 (denoted as Ru/Fe_2O_3–Li) was achieved by a wet impregnation method. The high-angle annular dark-field scanning TEM (HAADF-STEM) images in Fig. 1d clearly show that Ru clusters are randomly dispersed on the (110) surface of Fe_2O_3–Li. Fig. S4† shows that no new crystal phases were formed after Ru cluster decoration. Fig. 1e and S5† display the simulated lattice distortion of Ru/Fe_2O_3–Li by the geometric phase analysis (GPA) method, further indicating lattice expansion of
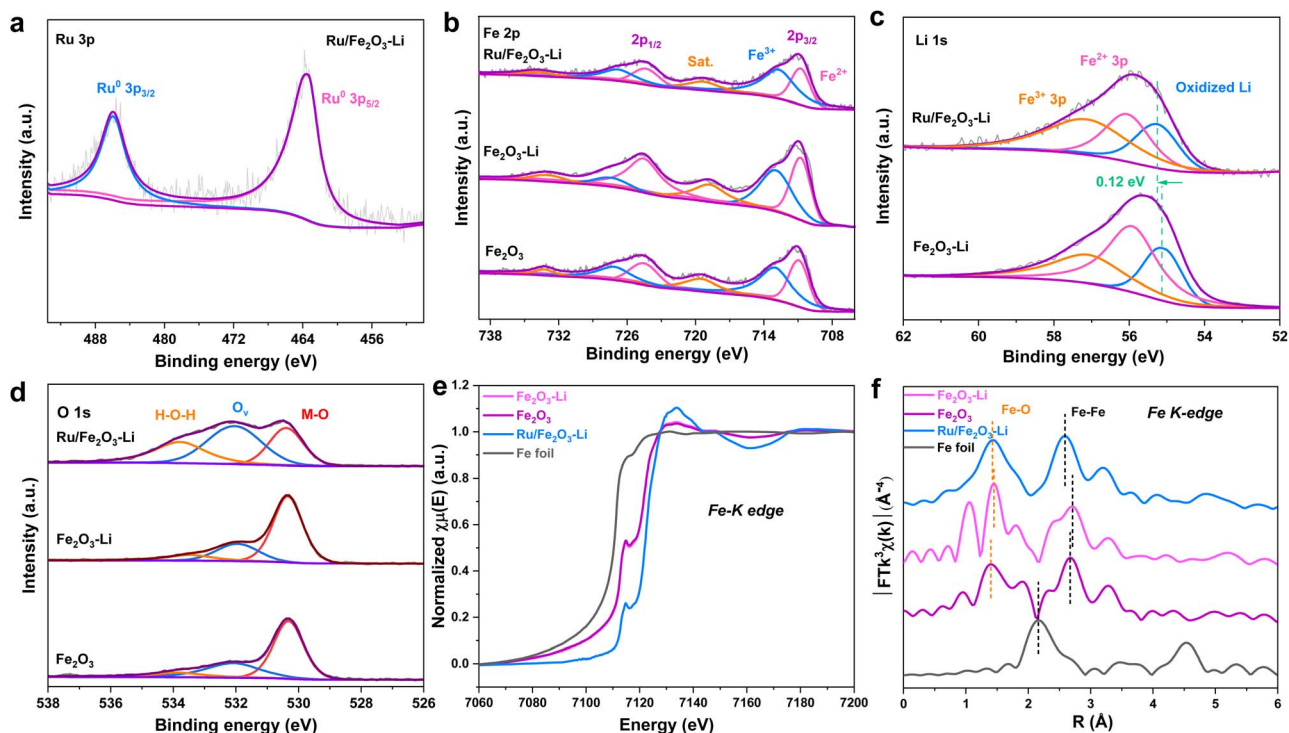

Fig. 2 Electronic properties and the coordination environment. (a) High-resolution XPS spectrum of Ru 3p for Ru/Fe_2O_3–Li. (b) High-resolution XPS spectra of Fe 2p for Fe_2O_3, Fe_2O_3–Li, and Ru/Fe_2O_3–Li. (c) High-resolution XPS spectra of Li 1s for Fe_2O_3–Li, and Ru/Fe_2O_3–Li. (d) High-resolution XPS spectra of O 1s for Fe_2O_3, Fe_2O_3–Li, and Ru/Fe_2O_3–Li. (e) Fe–K edge XANES spectra for Fe_2O_3, Fe_2O_3–Li, and Ru/Fe_2O_3–Li, Fe foil. (f) Radical distribution function of Fe–K edge XAFS spectra for Fe_2O_3, Fe_2O_3–Li, Ru/Fe_2O_3–Li, and Fe foil.

hematite Fe_2O_3 after Li ion insertion and Ru cluster decoration. The line-scan profile in Fig. S6† further indicates that the bright nanoparticles are Ru species. The energy-dispersive spectroscopic (EDS) elemental mapping images in Fig. 1f demonstrate the homogeneous distribution of Fe and O elements and the existence of the Ru element.

The high-resolution Ru 3p X-ray photoelectron spectroscopy (XPS) spectrum in Fig. 2a shows two peaks located at 463.5 and 486.0 eV, which are assigned to $3p_{5/2}$ and $3p_{3/2}$ of Ru^0, respectively.[30–32] In the high-resolution Fe 2p XPS spectra in Fig. 2b, two sets of triplet peaks were observed between 708 and 738 eV, which could be attributed to the doublet peaks of Fe^{2+} and Fe^{3+} and their satellite peaks.[33–35] In the high-resolution XPS spectra of Li 1s in Fig. 2c, the peak located at 55.1 eV in Fe_2O_3–Li was found to be oxidized Li.[36–38] Compared with Fe_2O_3–Li, the Li 1s peak in Ru/Fe_2O_3–Li shifted to higher binding energy by about 0.12 eV, indicating that electron depletion occurred on Li species in Ru/Fe_2O_3–Li after Ru cluster decoration. No obvious decrease in the Li amount was observed in the Li 1s XPS spectra for depth profiling analysis of Fe_2O_3–Li as the etching time increased (Fig. S7†), indicating that Li ions were mainly inserted into the hematite Fe_2O_3 bulk phase. In the high-resolution XPS spectra of O 1s in Fig. 2d, three peaks corresponding to the metal–oxygen (M–O) bond, H–O–H bond in surface adsorbed water, and oxygen vacancy (O_v) were observed. Compared with Fe_2O_3 and Fe_2O_3–Li, more O_v were formed after introducing Ru clusters, which is beneficial to dissociate H_2O molecules.[39,40]

We then performed X-ray absorption spectroscopy (XAS) to investigate the influence of Li ion insertion and Ru cluster decoration on the atomic structure and coordination environment of hematite Fe_2O_3 (Fig. 2e and f). The X-ray absorption near-edge spectroscopy (XANES) spectrum of Fe K-edge suggests that the Fe oxidation valence state in Fe_2O_3–Li and Fe_2O_3 (Fig. 2e) was lower than that in Ru/Fe_2O_3–Li. The corresponding extended X-ray absorption fine-structure (EXAFS) spectrum of Ru/Fe_2O_3–Li at the Fe K-edge in Fig. 2f shows a dominant peak at around 1.5 Å, which was assigned to the Fe–O coordination. Detailed analysis suggests that the length of the Fe–O bond in Ru/Fe_2O_3–Li and Fe_2O_3–Li was longer than that in Fe_2O_3, consistent with the above XRD refinement and HRTEM analysis.
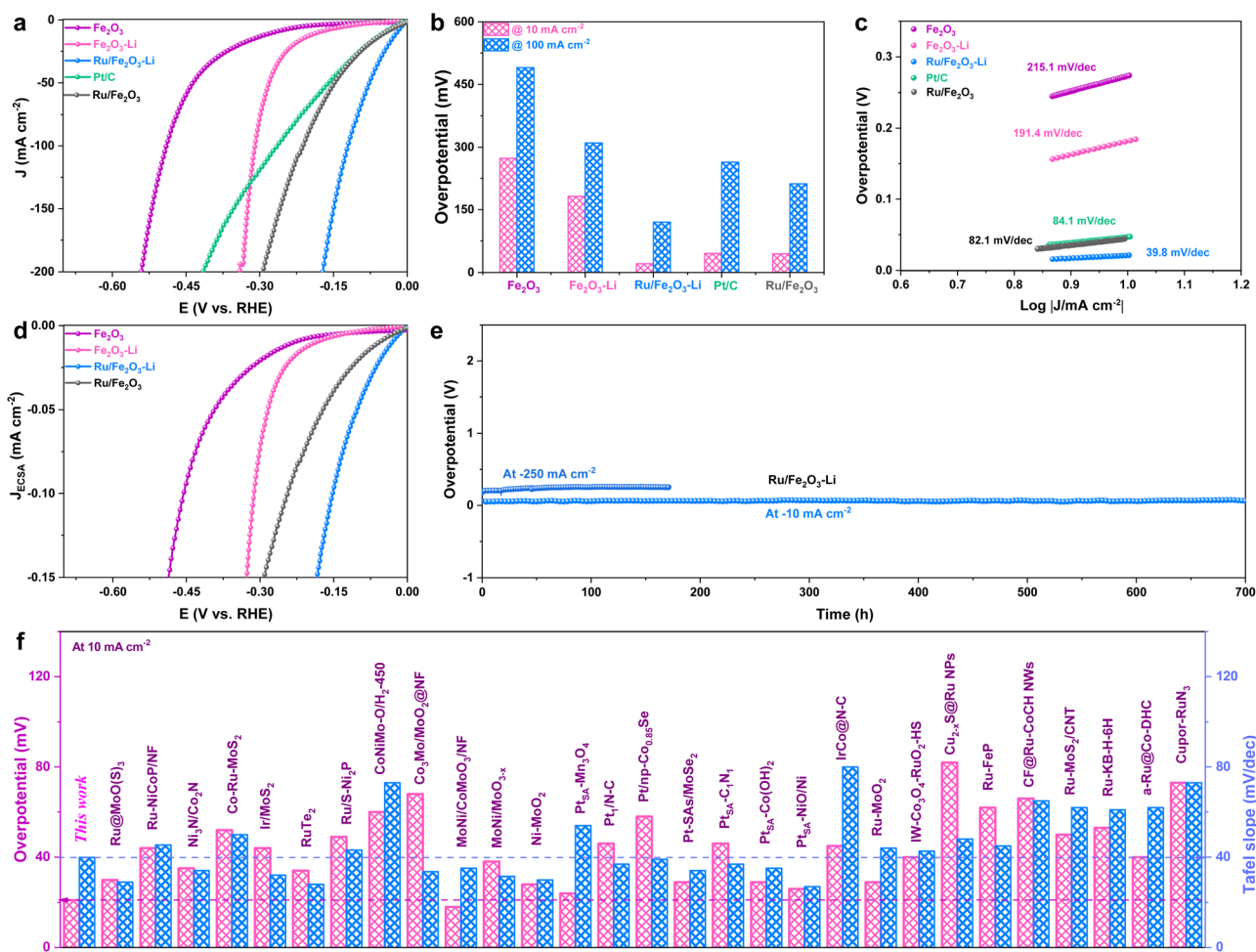

Fig. 3 Electrocatalytic HER performance evaluation. (a) LSV curves, (b) overpotential comparison, and (c) Tafel slope comparison of Fe_2O_3, Fe_2O_3–Li, Ru/Fe_2O_3, Ru/Fe_2O_3–Li and benchmark commercial Pt/C catalysts. Electrolyte: 1.0 M KOH. (d) ECSA-normalized LSV curves of Fe_2O_3, Fe_2O_3–Li, Ru/Fe_2O_3, and Ru/Fe_2O_3–Li. (e) Chronopotentiometry test of Ru/Fe_2O_3–Li at a current density of -10 mA cm^{-2} and -250 mA cm^{-2}. (f) Comparison of the overpotential at 10 mA cm^{-2} and Tafel slope values for Ru/Fe_2O_3–Li with that of recently reported catalysts for the HER in alkaline media.

HER performance evaluation in alkaline electrolyte

Following HER measurement protocols, we evaluated HER activities of Ru/Fe_2O_3–Li and control samples on a typical three-electrode set-up in 1.0 M KOH electrolyte. The control samples were Fe_2O_3–Li, Fe_2O_3, Ru/Fe_2O_3, and commercial Pt/C (denoted as Pt/C). Linear sweep voltammetry (LSV) curves in Fig. 3a show that Li ion insertion and Ru cluster decoration can effectively promote the electrocatalytic HER. As expected, Ru/Fe_2O_3–Li exhibits the best activity and is even better than Pt/C. The overpotential of Pt/C to deliver 10 mA cm^{-2} was 46 mV (Fig. 3b), consistent with previous reports.[16,31] Li ion insertion shows an obvious enhancement in the HER activity of hematite Fe_2O_3, and the overpotential for Fe_2O_3–Li to reach 10 mA cm^{-2} was 182 mV, lower than that of Fe_2O_3 (273 mV). The overpotential of Ru/Fe_2O_3–Li to drive 10 mA cm^{-2} was 21 mV, which is much lower than that of control catalysts. This difference was quickly increased with the increase of current density, due to the significantly smaller Tafel slope of Ru/Fe_2O_3–Li (39.8 mV dec^{-1}) than that of Ru/Fe_2O_3 (82.1 mV dec^{-1}), Fe_2O_3–Li (191.4 mV dec^{-1}) and Fe_2O_3 (215.1 mV dec^{-1}) (Fig. 3c). Electrochemical impedance spectroscopy (EIS) spectra of Ru/Fe_2O_3–Li at -0.02 V versus the reversible hydrogen electrode (RHE) displayed the lowest charge transfer resistance (Fig. S8†), suggesting enhanced HER kinetics compared with Ru/Fe_2O_3, Fe_2O_3–Li and Fe_2O_3.[41,42] The superior activity of Ru/Fe_2O_3–Li is among the best compared with recently reported HER catalysts (Fig. 3f and Table S1†).

To better understand the origin for enhanced HER performance of Ru/Fe_2O_3–Li, we first measured electrochemical double layer capacitance (C_{dl}) to calculate the electrochemically active surface area (ECSA) for specific activity analysis. Both Fe_2O_3–Li and Ru/Fe_2O_3 have higher C_{dl} values than Fe_2O_3 (Fig. S9†), suggesting that both Li insertion and Ru decoration can increase the ECSA and thus the number of catalytically active sites of Fe_2O_3. Consequently, Ru/Fe_2O_3–Li has the highest ECSA among all the samples. To investigate the intrinsic activity of Ru/Fe_2O_3–Li, the HER current density is normalized by ECSA to obtain the specific activity, which still follows the order: Ru/Fe_2O_3–Li > Ru/Fe_2O_3 > Fe_2O_3–Li > Fe_2O_3 (Fig. 3d), suggesting that Li intercalation and Ru decoration can promote the intrinsic catalytic activity. The influence of Li and Ru loading amounts on HER activity was also studied. Fig. S10† shows that the Fe_2O_3–Li catalyst with a lithiation time of 5 min and the Ru/Fe_2O_3–Li catalyst with a wet impregnation time of 2 min exhibited optimal activity. Apart from remarkable activity, good stability also plays an important role in alkaline water splitting.[43,44] The HER durability in alkaline electrolyte was evaluated at a current density of 10 mA cm^{-2} and 250 mA cm^{-2}. Our as-fabricated Ru/Fe_2O_3–Li presented a negligible potential increase after 700 h of continuous operation at 10 mA cm^{-2} and approaching 170 h of continuous operation at 250 mA cm^{-2} (Fig. 3e), confirming an excellent stability toward alkaline HER. After this stability test, the crystalline structure was retained (Fig. S11 and S12†) and no obvious element segregation was observed (Fig. S13†).

OER performance evaluation in alkaline electrolyte

The OER performance of Ru/Fe_2O_3–Li was also studied on a traditional three-electrode set-up in 1.0 M KOH electrolyte. The LSV curves in Fig. 4a showed that our as-synthesized Ru/Fe_2O_3–Li catalyst exhibited better OER activity than all the control samples, including Ru/Fe_2O_3, Fe_2O_3–Li, Fe_2O_3, and
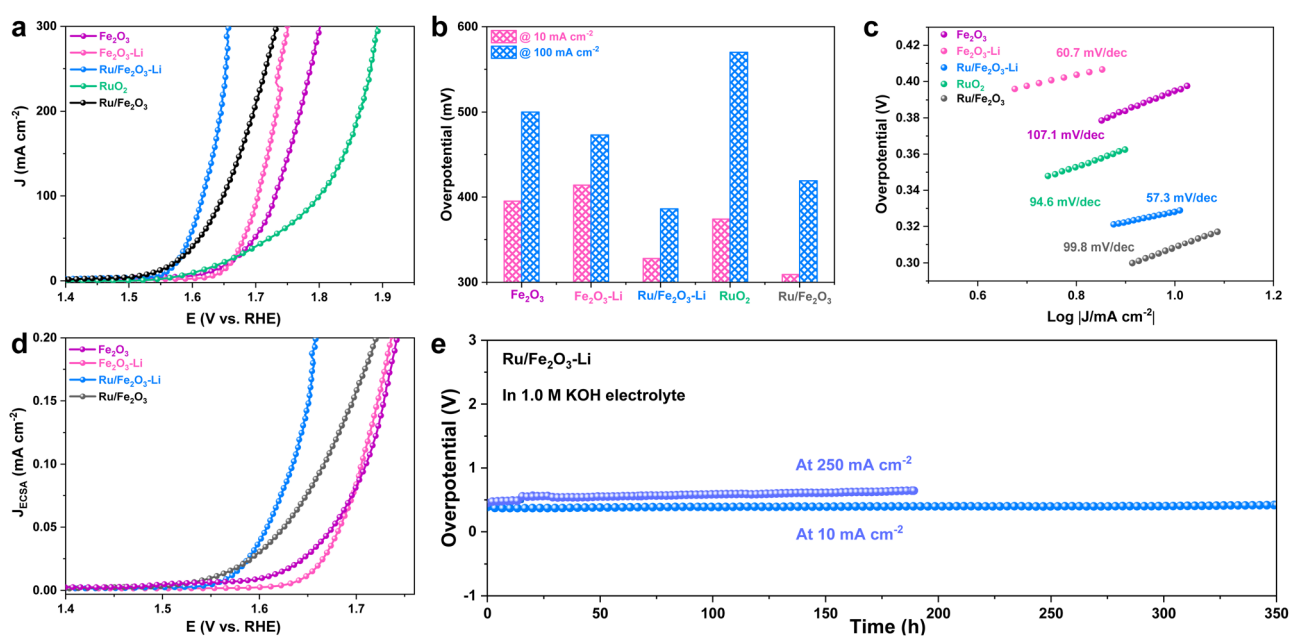

Fig. 4 Electrocatalytic OER performance evaluation. (a) LSV curves, (b) overpotential comparison, and (c) Tafel slope comparison of Fe_2O_3, Fe_2O_3–Li, Ru/Fe_2O_3, Ru/Fe_2O_3–Li and benchmark commercial RuO_2 catalysts. Electrolyte: 1.0 M KOH. (d) ECSA-normalized LSV curves of Fe_2O_3, Fe_2O_3–Li, Ru/Fe_2O_3, and Ru/Fe_2O_3–Li. (e) Chronopotentiometry test of the Ru/Fe_2O_3–Li catalyst at a current density of 10 mA cm^{-2} and 250 mA cm^{-2}.

commercial RuO_2. And the Fe_2O_3–Li catalyst presented enhanced OER activity compared to Fe_2O_3, indicating the effectiveness of Li ion intercalation. The overpotential of Ru/Fe_2O_3–Li to deliver a current density of 100 mA cm^{-2} was 386 mV (Fig. 4b), which is much lower than that of Ru/Fe_2O_3 (419 mV), Fe_2O_3–Li (473 mV) and Fe_2O_3 (500 mV). And the Tafel slope of Ru/Fe_2O_3–Li (57.3 mV dec^{-1}) decreased compared with that of Ru/Fe_2O_3 (99.8 mV dec^{-1}), Fe_2O_3–Li (60.7 mV dec^{-1}), Fe_2O_3 (107.1 mV dec^{-1}) and RuO_2 (94.6 mV dec^{-1}) (Fig. 4c). In addition, the ECSA-normalized current density in Fig. 4d suggests higher OER intrinsic activity of Ru/Fe_2O_3–Li compared with Ru/Fe_2O_3, Fe_2O_3–Li, Fe_2O_3. The influence of Li and Ru loading amounts on OER activity was also studied. Fig. S14† shows that the Fe_2O_3–Li catalyst with a lithiation time of 5 min and the Ru/Fe_2O_3–Li catalyst with a wet impregnation time of 2 min exhibited optimal activity. Furthermore, we studied the catalytic stability of Ru/Fe_2O_3–Li toward alkaline OER. A negligible voltage increase was observed during the 350-h measurement at 10 mA cm^{-2} and 190-h measurement (Fig. 4e) at 250 mA

cm^{-2}, indicating its electrochemical robustness toward the OER. The morphology and crystal structure of Ru/Fe_2O_3–Li maintained after the stability test (Fig. S15 and S16†), confirming its satisfactory structural stability. The intensified M–O bonds in O 1s XPS spectra and weakened Li–O bonds in Li 1s XPS spectra of Ru/Fe_2O_3–Li after the OER stability test (Fig. S17†) were probably ascribed to the surface reconstruction process during OER operating potential.

Understanding the mechanism for enhanced HER/OER kinetics

To elucidate the origin of Li ion insertion and subsequently Ru cluster decoration for enhanced catalysis theoretically, we performed density functional theory (DFT) calculations. According to our XRD observation, the Fe_2O_3 crystals were modeled with a hematite lattice structure. The (110) facet of hematite Fe_2O_3 is commonly exposed on the surface (Fig. 1d); hence it is chosen for simulations. In the simulated model, the bottom has several
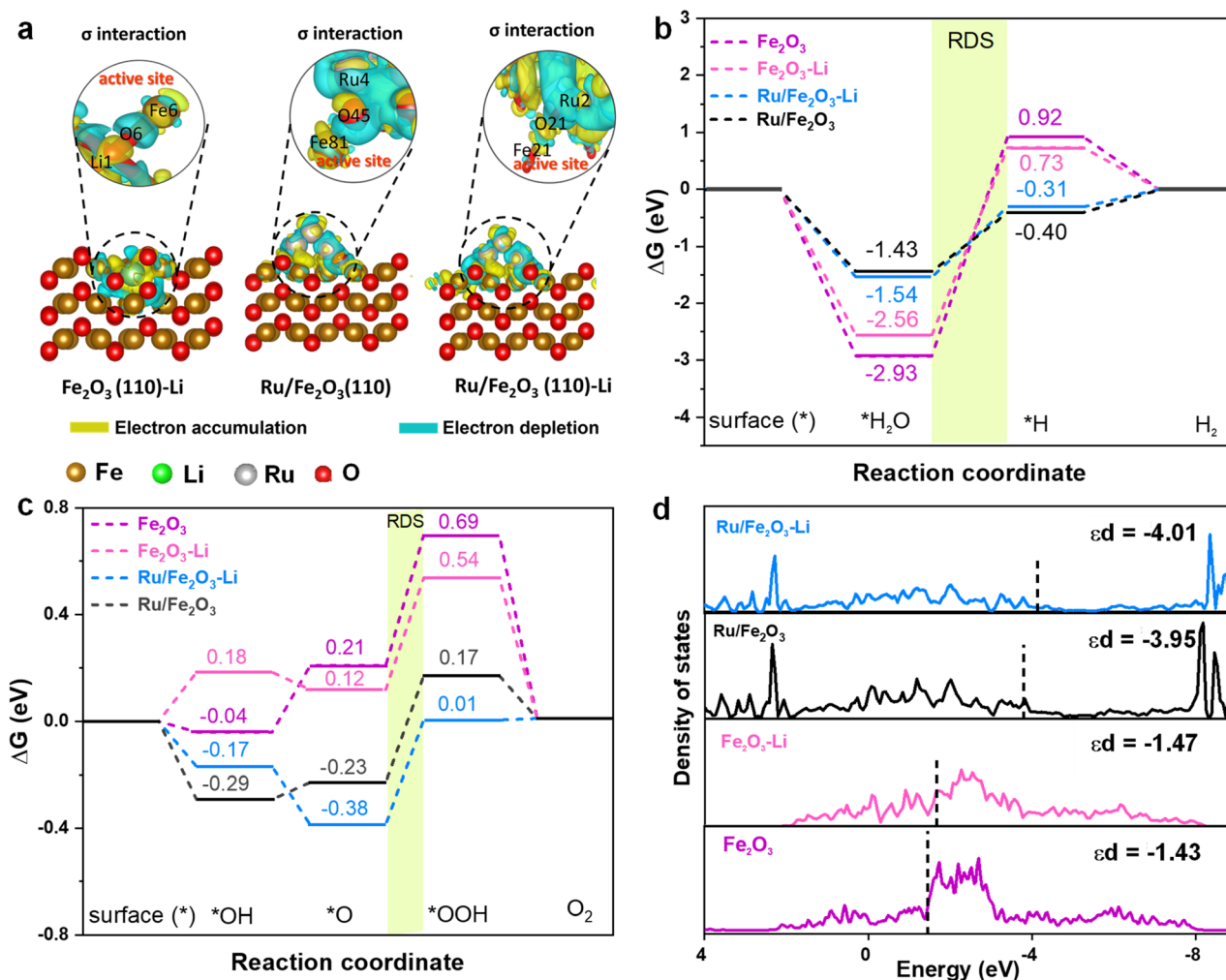

Fig. 5 DFT calculations. (a) Charge density difference analysis of Fe_2O_3–Li, Ru/Fe_2O_3 and Ru/Fe_2O_3–Li. (b) Gibbs free energy difference comparison of the alkaline HER pathway for Fe_2O_3, Fe_2O_3–Li, Ru/Fe_2O_3, and Ru/Fe_2O_3–Li. (c) Gibbs free energy difference comparison of the alkaline OER pathway for Fe_2O_3, Fe_2O_3–Li, Ru/Fe_2O_3 and Ru/Fe_2O_3–Li. (d) PDOS analysis and the calculated d-band center values of active Fe cations for Fe_2O_3, Fe_2O_3–Li, Ru/Fe_2O_3 and Ru/Fe_2O_3–Li.

layers of equivalent Fe_2O_3 units, with one Fe atom on topmost being replaced by a Li atom (Fig. 5a). This Li-intercalated Fe_2O_3 surface was employed to investigate the impact of Li ion insertion on the HER/OER process. Another molecular model uses the above Li-inserted Fe_2O_3 surface as the substrate, decorated with Ru clusters consisting of 6 Ru atoms, to investigate the synergistic effect of Li ion intercalation and Ru cluster incorporation on the HER/OER process. The Ru/Fe_2O_3 model without Li ion insertion was also employed for comparison.

The schematic representation in Fig. 5a illustrates the charge density difference of Ru/Fe_2O_3, Fe_2O_3–Li and Ru/Fe_2O_3–Li. The local Fe cation accumulated electrons, stemming from Li ion insertion and Ru cluster decoration. The impacts of Li ion insertion and subsequently Ru cluster decoration on catalytic activity were evaluated by considering the limiting potential calculations. For the HER, Fig. S18† shows the DFT-tested optimal sites for *H adsorption on Fe_2O_3 (110), Fe_2O_3 (110)–Li, Ru/Fe_2O_3 (110), and Ru/Fe_2O_3 (110)–Li models. Fig. 5b illustrates the free energy evolution for the HER on pure Fe_2O_3 (110), Ru cluster decorated Fe_2O_3 (110), Li-intercalated Fe_2O_3

(110), and Ru cluster decorated Fe_2O_3 (110)–Li surfaces. The rate-determining step (RDS) for the HER on these surfaces was predicted to be the transformation of *H_2O into *H, *i.e.* the water molecule dissociation step in alkaline HER, aligning with previous results.[45,46] The predicted limiting potential for the HER on Ru/Fe_2O_3–Li (1.23 eV) was lower than that of Fe_2O_3–Li (3.29 eV) and Fe_2O_3 (3.85 eV), suggesting improved HER activity, in line with our experimental findings. The stronger *H_2O adsorption energy (−1.54 eV) and moderate *H adsorption energy (−0.31 eV) on Ru/Fe_2O_3–Li than those of Ru/Fe_2O_3 (−1.43 eV for *H_2O adsorption and −0.40 eV for *H adsorption, respectively) indicate enhanced H_2O molecule adsorption and H_2 molecule release on Ru/Fe_2O_3–Li, and thus promoted alkaline HER activity was obtained.[47] As for the OER, Fig. S19–S22† display the DFT-tested optimal active sites on Fe_2O_3 (110), Fe_2O_3 (110)–Li, Ru/Fe_2O_3 (110) and Ru/Fe_2O_3 (110)–Li models. Fig. 5c illustrates the free energy evolution for the OER on the Fe_2O_3 (110), Fe_2O_3 (110)–Li, Ru/Fe_2O_3 (110), and Ru/Fe_2O_3 (110)–Li surfaces. The RDS for the OER on the above three surfaces was predicted to be the transformation of *O into *OOH, consistent
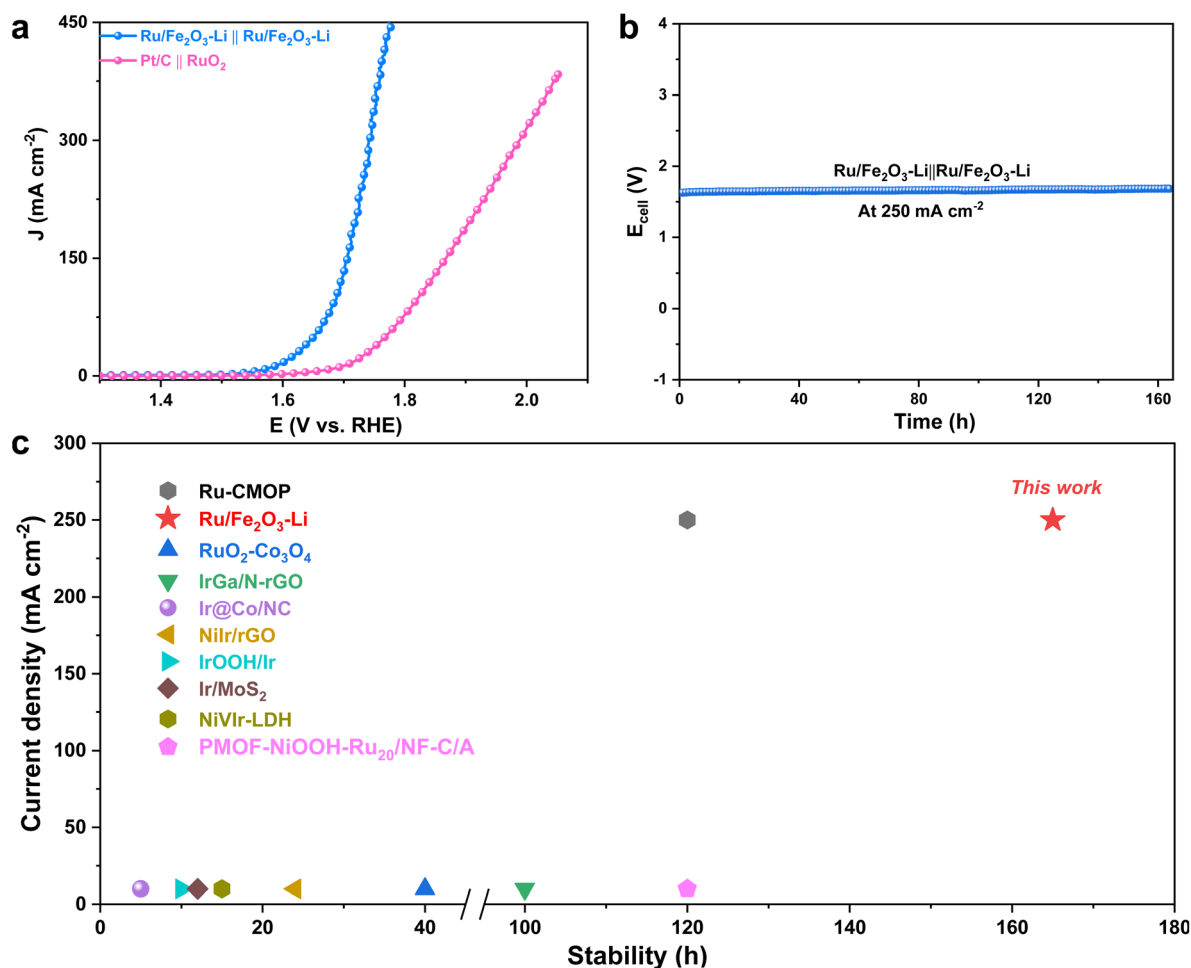

Fig. 6 Electrocatalytic overall water splitting performance evaluation. (a) LSV curves of Ru/Fe_2O_3–Li‖Ru/Fe_2O_3–Li and the benchmark pair of the commercial $Pt/C‖RuO_2$ system. Electrolyte: 1.0 M KOH. (b) Chronopotentiometry test of the Ru/Fe_2O_3–Li‖Ru/Fe_2O_3–Li system at a current density of 250 mA cm^{-2} in 1.0 M KOH electrolyte. (c) Comparison of catalytic stability of Ru/Fe_2O_3–Li‖Ru/Fe_2O_3–Li with that of recently reported bifunctional catalysts for overall water splitting in alkaline media.

with previous reports.[41,48,49] The predicted limiting potential for the OER on Ru/Fe$_2$O$_3$–Li (0.39 eV) was lower than that of Ru/Fe$_2$O$_3$ (0.40 eV), Fe$_2$O$_3$–Li (0.42 eV) and Fe$_2$O$_3$ (0.48 eV), suggesting enhanced OER activity, in line with our experimental findings.

The promoted HER/OER performance is explained by the projected density of states (PDOS) of the d orbitals[50,51] of the Fe atom, which interact with the intermediates. As shown in Fig. 5d, the DFT-calculated d-band centers of Fe$_2$O$_3$–Li, Ru/Fe$_2$O$_3$, and Ru/Fe$_2$O$_3$–Li shifted to lower energy levels away from Fermi energy by 0.04 eV, 2.52 eV and 2.58 eV compared with that of Fe$_2$O$_3$, respectively, which is consistent with the charge density difference analysis in Fig. 5a. The PDOS shifts to lower energy levels for Ru/Fe$_2$O$_3$–Li, which is beneficial to increase the intrinsic activity of hematite Fe$_2$O$_3$ for the HER and OER.[52,53] Consequently, our DFT simulations indicate that Li ion insertion and subsequent Ru cluster decoration improve both the HER and OER kinetics of hematite Fe$_2$O$_3$ by influencing the electronic structure of active Fe cation, supporting our experimental observations. As for the stability, we carefully calculated the interaction between Ru clusters and the Li ion intercalated Fe$_2$O$_3$ (110) support (Fig. S23†). The interaction between Ru clusters and Fe$_2$O$_3$ (110)–Li is 1.6 eV stronger than that between Ru clusters and pristine Fe$_2$O$_3$ (110), and the structure of the Ru/Fe$_2$O$_3$ (110)–Li slab is more stable than that of Ru/Fe$_2$O$_3$ (110), further indicating that introducing Li ions into hematite Fe$_2$O$_3$ leads to strong metal–support interaction in this system, verifying the structural robustness and catalytic stability of our Ru/Fe$_2$O$_3$–Li heterostructure.

Electrolyzer performance evaluation

To investigate the practical application potential of our Ru/Fe$_2$O$_3$–Li catalyst for hydrogen production, we assembled an electrolyzer using Ru/Fe$_2$O$_3$–Li as both the anode and cathode. The LSV curves in Fig. 6a showed that the Ru/Fe$_2$O$_3$–Li‖Ru/Fe$_2$O$_3$–Li system exhibited significantly enhanced activity toward overall water splitting, only requiring 1.68 V to deliver 100 mA cm^{-2}, which was much lower than that (1.82 V) of the benchmark pair of Pt/C‖RuO$_2$ at the same current density. Considering the importance of catalytic stability in practical application, we thus evaluated the stability of our as-fabricated Ru/Fe$_2$O$_3$–Li catalyst. A negligible potential increase was observed during the 165-h chronopotentiometry test at 250 mA cm^{-2} in 1.0 M KOH electrolyte (Fig. 6b), indicating the robustness of our Ru/Fe$_2$O$_3$–Li catalyst toward overall water splitting. This performance outperforms most of that in recently reported studies on alkaline water electrolysis (Fig. 6c).

Conclusion

In summary, we developed a Ru cluster decorated and Li ion intercalated hematite Fe$_2$O$_3$ catalyst for water splitting in alkaline media. This Ru/Fe$_2$O$_3$–Li catalyst exhibited significantly enhanced performance toward the HER and OER compared with Ru/Fe$_2$O$_3$, Fe$_2$O$_3$–Li and Fe$_2$O$_3$. The systematic experimental characterization detailedly revealed the changes in atomic and electronic structures after Li ion insertion and subsequent Ru cluster decoration. Lattice expansion of crystalline hematite Fe$_2$O$_3$ was observed after Li ion insertion, and complex electron transfer phenomena occurred due to the synergistic effect between Ru clusters and Li-intercalated hematite Fe$_2$O$_3$. Theoretical calculations indicated that the band gap of semiconductor hematite Fe$_2$O$_3$ narrowed after lithiation, and the electronic and lattice distortion effects promoted catalysis synergistically on Ru/Fe$_2$O$_3$–Li. This work suggests that lithiation of the oxide support could be an effective strategy to enhance the catalytic performance of heterostructured nanomaterials.

Data availability

The data supporting the findings of this work are available within the article and its ESI.† Raw data supporting the findings of this work are available from the corresponding author upon reasonable request.

Author contributions

H. Ma, J. Ma and H. Cheng conceived the research project. J. Ma and H. Cheng supervised the project. H. Ma designed the catalysts, performed most of experimental section and conducted detailed analysis of the experimental data. Y. Yang and X. Yu performed the density functional theory simulations and provided solid evidence to explain the experimental findings. Y. Yang assisted to complete all the XAS experiments in this work and provided much assistance in XAS data analysis. Y. Zhao conducted the spherical aberration corrected transmission electron microscope test, analyzed the relevant characterization results in detail and provided many insightful suggestions to improve this work.

Conflicts of interest

There are no conflicts to declare.

Acknowledgements

References

1 J. A. Turner, Sustainable hydrogen production, *Science*, 2004, **305**, 972–974.

2 S. Chu and A. Majumdar, Opportunities and challenges for a sustainable energy future, *Nature*, 2012, **488**, 294–303.

3 Z. W. Seh, J. Kibsgaard, C. F. Dickens, I. Chorkendorff, J. K. Nørskov and T. F. Jaramillo, Combining theory and experiment in electrolysis: Insights into materials design, *Science*, 2017, **355**, eaad4998.

4 J. Wei, M. Zhou, A. Long, Y. Xue, H. Liao, C. Wei and Z. J. Xu, Heterostructured electrocatalysts for hydrogen evolution reaction under alkaline conditions, *Nano-Micro Lett.*, 2018, **10**, 75.

5 Z. He, C. Zhang, S. Guo, P. Xu, Y. Ji, S. Luo, X. Qi, Y. Liu, N. Cheng, S. Dou, Y. Wang and B. Zhang, Mn-doping heterojunction: interfacial engineering in an efficient electrocatalyst for superior simulated seawater hydrogen evolution, *Chem. Sci.*, 2024, **15**, 1123–1131.

6 C. Liu and L. Feng, Chin. Advances in anode catalysts of methanol-assisted water splitting reactions for hydrogen generation, *J. Struct. Chem.*, 2023, **42**, 100136.

7 Q. Xue, Z. Wang, Y. Ding, F. Li and Y. Chen, Chemical functionalized noble metal nanocrystals for electrocatalysis, *Chin. J. Catal.*, 2023, **45**, 6–16.

8 X. Liu, Y. Jiang, J. Huang, W. Zhong, B. He, P. Jin and Y. Chen, Bifunctional PdPt bimetallenes for formate oxidation-boosted water electrolysis, *Carbon Energy*, 2023, **5**, e367.

9 Y. Yan, T. He, B. Zhao, K. Qi, H. Liu and B. Y. Xia, Metal/covalent-organic frameworks-based electrolytes for water splitting, *J. Mater. Chem. A*, 2018, **6**, 15905.

10 J. Pan, Y. Y. Xu, H. Yang, Z. Dong, H. Liu and B. Y. Xia, Advanced architectures and relatives of air electrodes in Zn-air batteries, *Adv. Sci.*, 2018, **5**, 1700691.

11 X. Yu, J. Zhao and M. Johnsson, Interfacial engineering of nickel hydroxide on cobalt phosphide for alkaline water electrolysis, *Adv. Funct. Mater.*, 2021, **31**, 2101578.

12 N. Mahmood, Y. Yao, J. W. Zhang, L. Pan, X. Zhang and J. J. Zou, Electrocatalysts for hydrogen evolution in alkaline electrolytes: mechanisms, challenges, and prospective solutions, *Adv. Sci.*, 2018, **5**, 1700464.

13 H. Ma, X. Zhou, J. Li, H. Cheng and J. Ma, Rational design of heterostructured nanomaterials for accelerating electrocatalytic hydrogen evolution reaction kinetics in alkaline media, *J. Electrochem.*, 2024, **30**, 2305101.

14 L. Chong, G. Gao, J. Wen, H. Li, H. Xu, Z. Green, J. D. Sugar, A. J. Kropf, W. Xu, X. Lin, H. Xu, L. Wang and D. Liu, La- and Mn-doped cobalt spinel oxygen evolution catalyst for proton exchange membrane electrolysis, *Science*, 2023, **380**, 609–616.

15 J. Suntivich, K. J. May, H. A. Gasteiger, J. B. Goodenough and Y. Shao-horn, A perovskite oxide optimized for oxygen evolution catalysis from molecular orbital principles, *Science*, 2011, **334**, 1383–1385.

16 H. Ma, Z. Chen, Z. Wang, C. V. Singh and Q. Jiang, Interface engineering of Co/CoMoN/NF heterostructures for high-performance electrochemical overall water splitting, *Adv. Sci.*, 2022, **9**, 2105313.

17 B. Zhang, L. Zhang, Q. Tan, J. Wang, J. Liu, H. Wan, L. Miao and J. Jiang, Simultaneous interfacial chemistry and inner Helmholtz plane regulation for superior alkaline hydrogen evolution, *Energy Environ. Sci.*, 2020, **13**, 3007–3013.

18 J. Zhang, J. Qian, J. Ran, P. Xi, L. Yang and D. Gao, Engineering lower coordination atoms onto NiO/Co_3O_4 heterointerfaces for boosting oxygen evolution reactions, *ACS Catal.*, 2020, **10**, 12376–12384.

19 B. Zhang, J. Wang, G. Liu, C. M. Weiss, D. Liu, Y. Chen, L. Xia, P. Zhou, M. Gao, Y. Liu, J. Chen, Y. Yan, M. Shao, H. Pan and W. Sun, A strongly coupled Ru-CrO_x cluster-cluster heterostructure for efficient alkaline hydrogen electrocatalysis, *Nat. Catal.*, 2024, **7**, 441–451.

20 R. Liu, M. Sun, X. Liu, Z. Lv, X. Yu, J. Wang, Y. Liu, L. Li, X. Feng, W. Yang, B. Huang and B. Wang, Enhanced metal-support interactions boost the electrocatalytic water splitting of supported ruthenium nanoparticles on a Ni_3N/NiO heterojunction at industrial current density, *Angew. Chem., Int. Ed.*, 2023, **62**, e202312644.

21 Y. Qin, T. Yu, S. Deng, X. Zhou, D. Lin, Q. Zhang, Z. Jin, D. Zhang, Y. He, H. Qiu, L. He, F. Kang, K. Li and T. Zhang, RuO_2 electronic structure and lattice strain dual engineering for enhanced acidic oxygen evolution reaction performance, *Nat. Commun.*, 2022, **13**, 3784.

22 B. You, M. T. Tang, C. Tsai, F. Ablid-Pedersen, X. Zheng and H. Li, Enhancing electrocatalytic water splitting by strain engineering, *Adv. Mater.*, 2019, **31**, 1807001.

23 S. Hao, H. Sheng, M. Liu, J. Huang, G. Zheng, F. Zhang, X. Liu, Z. Su, J. Hu, Y. Qian, L. Zhou, Y. He, B. Song, L. Lei, X. Zhang and S. Jin, Torsion strained iridium oxide for efficient acidic water oxidation in proton exchange membrane electrolyzers, *Nat. Nanotechnol.*, 2021, **16**, 1371–1377.

24 Y. Hu, Y. Pan, Z. Wang, T. Lin, Y. Gao, B. Luo, H. Hu, F. Fan, G. Liu and L. Wang, Lattice distortion induced internal electronic field in TiO_2 photoelectrode for efficient charge separation and transfer, *Nat. Commun.*, 2020, **11**, 2129.

25 C. Ghosh, M. K. Singh, S. Parida, M. T. Janish, A. Dobley, A. M. Dongare and C. B. Carter, Phase evolution and structural modulation during in situ lithiation of MoS_2, WS_2 and graphite in TEM, *Sci. Rep.*, 2021, **11**, 9014.

26 S. Yan, C. Peng, C. Yang, Y. Chen, J. Zhang, A. Guan, X. Lv, H. Wang, Z. Wang, T. Sham, Q. Han and G. Zheng, Electron localization and lattice strain induced by surface lithium doping enable ampere-level electrosynthesis of formate from CO_2, *Angew. Chem., Int. Ed.*, 2021, **60**, 25741–25745.

27 T. Liu, J. Liu, L. Li, L. Yu, J. Diao, T. Zhou, S. Li, A. Dai, W. Zhao, S. Xu, Y. Ren, L. Wang, T. Wu, R. Qi, Y. Xiao, J. Zheng, W. Cha, R. Harder, I. Robinson, J. Wen, J. Lu, F. Pan and K. Amine, Origin of structural degradation in Li-rich layered oxide cathode, *Nature*, 2022, **606**, 305–312.

28 L. Jin, C. Shen, Q. Wu, A. Shellikeri, J. Zheng, C. Zhang and J. P. Zheng, Pre-lithiation strategies for next-generation practical lithium-ion batteries, *Adv. Sci.*, 2021, **8**, 2005031.

29 A. Chaves, J. G. Azadani, H. Alsalman, D. R. da Costa, R. Frisenda, A. J. Chaves, S. H. Song, Y. D. Kim, D. He, J. Zhou, A. Castellanos-Gomez, F. M. Peeters, Z. Liu, C. L. Hinkle, S. Oh, P. D. Ye, S. J. Koester, Y. H. Lee, P. Avouris, X. Wang and T. Low, Bandgap engineering of two-dimensional semiconductor materials, *npj 2D Mater. Appl.*, 2020, **4**, 29.

30 Z. Wu, Q. Li, G. Xu, W. Jin, W. Xiao, Z. Li, T. Ma, S. Feng and L. Wang, Micro-wave phosphine-plasma-assisted ultrafast synthesis of halogen-doped Ru/RuP_2 with surface intermediate adsorption modulation for efficient alkaline hydrogen evolution reaction, *Adv. Mater.*, 2023, 231108.

31 K. Jiang, M. Luo, Z. Liu, M. Peng, D. Chen, Y. Lu, T. Chan, F. M. F. de Groot and Y. Tan, Rational strain engineering of single-atom ruthenium on nanoporous MoS_2 for highly efficient hydrogen evolution, *Nat. Commun.*, 2021, **12**, 1687.

32 H. Qi, J. Yang, F. Liu, L. Zhang, J. Yang, X. Liu, L. Li, Y. Su, Y. Liu, R. Hao, A. Wang and T. Zhang, Highly selective and robust single-atom catalyst Ru_1/NC for reductive animation of aldehydes/ketones, *Nat. Commun.*, 2021, **12**, 3295.

33 T. Marshall-Roth, N. J. Libretto, A. T. Wrobel, K. J. Anderton, M. L. Pegis, N. D. Ricke, T. V. Voorhis, J. T. Miller and Y. Surendranath, A pyridinic $Fe-N_4$ macrocycle models the active sites in Fe/N-doped carbon electrocatalysts, *Nat. Commun.*, 2020, **11**, 5283.

34 H. Kohzadi and M. Soleiman-Beigi, XPS and structural studies of Fe_3O_4-PTMS-NAS@Cu as a novel magnetic natural asphalt base network and recoverable nanocatalyst for the synthesis of biaryl compounds, *Sci. Rep.*, 2021, **11**, 24508.

35 M. Gong, Y. Li, H. Wang, Y. Liang, J. Z. Wu, J. Zhou, J. Wang, T. Regier, F. Wei and H. Dai, An advanced Ni-Fe layered double hydroxide electrocatalyst for water oxidation, *J. Am. Chem. Soc.*, 2013, **135**, 8452–8455.

36 S. Narayanan, U. Ulissi, J. S. Gibson, Y. A. Chart, R. S. Weatherup and M. Pasta, Effect of current density on the solid electrolyte interphase formation at the lithium/Li_6PS_5Cl interface, *Nat. Commun.*, 2022, **13**, 7237.

37 H. Sun, G. Zhu, Y. Zhu, M. Lin, H. Chen, Y. Li, W. H. Hung, B. Zhou, X. Wang, Y. Bai, M. Gu, C. Huang, H. Tai, X. Xu, M. Angell, J. Shyue and H. Dai, High-safety and high-energy-density lithium metal batteries in a novel ionic-liquid electrolyte, *Adv. Mater.*, 2020, **32**, 2001741.

38 K. N. Wood, K. X. Steirer, S. E. Hafner, C. Ban, S. Santhanagopalan, S. Lee and G. Teeter, Operando X-ray photoelectron spectroscopy of solid electrolyte interface formation and evolution in $Li_2S-P_2S_5$ solid-state electrolytes, *Nat. Commun.*, 2018, **9**, 2490.

39 K. Wang, S. Wang, K. S. Hui, J. Li, C. Zha, D. A. Dinh, Z. Shao, B. Yan, Z. Tang and K. N. Hui, Dense platinum/nickel oxide heterointerfaces with abundant oxygen vacancies enable ampere-level current density ultrastable hydrogen evolution in alkaline, *Adv. Funct. Mater.*, 2023, **33**, 2211273.

40 X. Li, W. Deng, Y. Weng, J. Zhang, H. Mao, T. Lu, W. Zhang, R. Yang and F. Jiang, Implanting H_xYO_{2-x} sites into Ru-doped graphene and oxygen vacancies for low-overpotential alkaline hydrogen evolution, *NPG Asia Mater.*, 2023, **15**, 55.

41 S. Hao, M. Liu, J. Pan, X. Liu, X. Tan, N. Xu, Y. He, L. Lei and X. Zhang, Dopants fixation of ruthenium for boosting acidic oxygen evolution stability and activity, *Nat. Commun.*, 2020, **11**, 5368.

42 Z. L. Zhao, Q. Wang, X. Huang, Q. Feng, S. Gu, Z. Zhang, H. Xu, L. Zeng, M. Gu and H. Li, Boosting the oxygen evolution reaction using defect-rich ultrathin ruthenium oxide nanosheets in acidic media, *Energy Environ. Sci.*, 2020, **13**, 5143–5151.

43 F. Chen, Z. Wu, Z. Adler and H. Wang, Stability challenges of electrocatalytic oxygen evolution reaction: from mechanistic understanding to reactor design, *Joule*, 2021, **5**, 1704–1731.

44 S. Geiger, O. Kasian, M. Ledendecker, E. Pizzutilo, A. M. Mingers, W. T. Fu, O. Diaz-Morales, Z. Li, T. Oellers, L. Fruchter, A. Ludwig, K. J. J. Mayrhofer, M. T. M. Koper and S. Cherevko, The stability number as a metric for electrocatalyst stability benchmarking, *Nat. Catal.*, 2018, **1**, 508–515.

45 R. Subbaraman, D. Tripkovic, D. Strmcnik, K. Chang, M. Uchimura, A. P. Paulikas, V. Stamenkovic and N. M. Markovic, Enhancing hydrogen evolution activity in water splitting by tailoring Li^+-$Ni(OH)_2$-Pt interfaces, *Science*, 2011, **334**, 1256–1260.

46 J. Hu, C. Zhang, L. Jiang, H. Lin, Y. An, D. Zhou, M. K. H. Leung and S. Yang, Nanohybridization of MoS_2 with layered double hydroxides efficiently synergizes the hydrogen evolution in alkaline media, *Joule*, 2017, **1**, 383–393.

47 R. Zhang, Y. Li, X. Zhou, A. Yu, Q. Huang, T. Xu, L. Zhu, P. Peng, S. Song, L. Echegoyen and F. Li, Single atomic platinum on fullerene C60 surfaces for accelerated alkaline hydrogen evolution, *Nat. Commun.*, 2023, **14**, 2460.

48 S. Chen, H. Huang, P. Jiang, K. Yang, J. Diao, S. Gong, S. Liu, M. Huang, H. Wang and Q. Chen, Mn-doped RuO_2 nanocrystals as highly active electrocatalysts for enhanced oxygen evolution in acidic media, *ACS Catal.*, 2020, **10**, 1152–1160.

49 Z. Wu, F. Chen, B. Li, S. Yu, Y. Z. Finfrock, D. M. Meira, Q. Yan, P. Zhu, M. Chen, T. Song, Z. Yin, H. Liang, S. Zhang, G. Wang and H. Wang, Non-iridium based electrocatalyst for durable acidic oxygen evolution reaction in proton exchange membrane water electrolysis, *Nat. Mater.*, 2023, **22**, 100–108.

50 J. K. NØrskov, Chemisorption on metal surfaces, *Rep. Prog. Phys.*, 1990, **53**, 1253.

51 J. K. NØrskov, Electronic factors in catalysis, *Prog. Surf. Sci.*, 1991, **38**, 103–144.

52 J. Li, Oxygen evolution reaction in energy conversion and storage: design strategies under and beyond the energy scaling relationship, *Nano-Micro Lett.*, 2022, **14**, 112.

53 X. Wang, Y. Zheng, W. Sheng, Z. J. Xu, M. Jaroniec and S. Qiao, Strategies for design of electrocatalysts for hydrogen evolution under alkaline conditions, *Mater. Today*, 2020, **36**, 125–138.